

## A dual wavelength imaging system for plasma-surface interaction studies on the National Spherical Torus Experiment Upgrade

F. Scotti and V. A. Soukhanovskii

Citation: *Review of Scientific Instruments* **86**, 123103 (2015); doi: 10.1063/1.4935609

View online: <http://dx.doi.org/10.1063/1.4935609>

View Table of Contents: <http://scitation.aip.org/content/aip/journal/rsi/86/12?ver=pdfcov>

Published by the [AIP Publishing](#)

---

### Articles you may be interested in

[Full toroidal imaging of non-axisymmetric plasma material interaction in the National Spherical Torus Experiment divertora\)](#)

Rev. Sci. Instrum. **83**, 10E532 (2012); 10.1063/1.4739510

[Snowflake divertor configuration studies in National Spherical Torus Experimenta\)](#)

Phys. Plasmas **19**, 082504 (2012); 10.1063/1.4737117

[Edge transport and turbulence reduction with lithium coated plasma facing components in the National Spherical Torus Experiment a\)](#)

Phys. Plasmas **18**, 056118 (2011); 10.1063/1.3592519

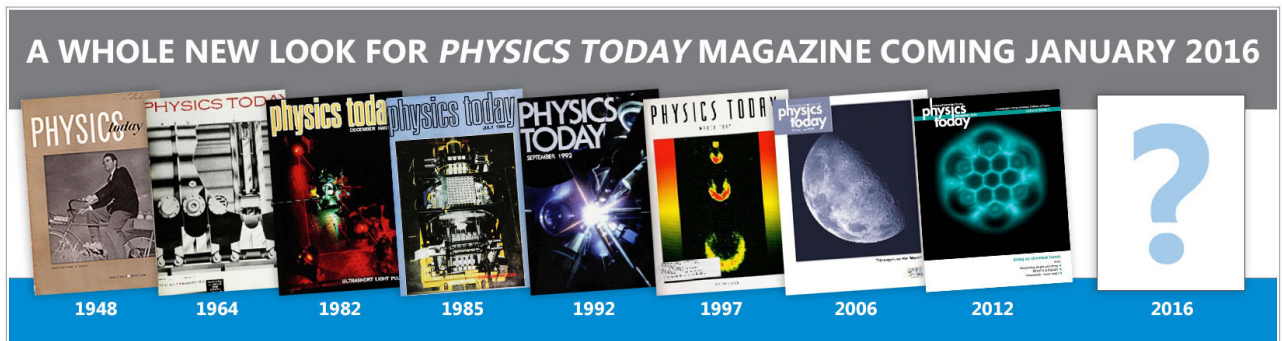
[Survey of diagnostic systems for the study of gyrocenter shifts on National Spherical Torus Experiment](#)

Rev. Sci. Instrum. **77**, 10F505 (2006); 10.1063/1.2220079

[Resistive wall mode stabilization of high- \$\beta\$  plasmas in the National Spherical Torus Experimenta\)](#)

Phys. Plasmas **12**, 056112 (2005); 10.1063/1.1883668

---



# A dual wavelength imaging system for plasma-surface interaction studies on the National Spherical Torus Experiment Upgrade

F. Scotti and V. A. Soukhanovskii

Lawrence Livermore National Laboratory, Livermore, California 94551, USA

(Received 26 June 2015; accepted 20 October 2015; published online 9 December 2015)

A two-channel spectral imaging system based on a charge injection device radiation-hardened intensified camera was built for studies of plasma-surface interactions on divertor plasma facing components in the National Spherical Torus Experiment Upgrade (NSTX-U) tokamak. By means of commercially available mechanically referenced optical components, the two-wavelength setup images the light from the plasma, relayed by a fiber optic bundle, at two different wavelengths side-by-side on the same detector. Remotely controlled filter wheels are used for narrow bandpass and neutral density filters on each optical path allowing for simultaneous imaging of emission at wavelengths differing in brightness up to 3 orders of magnitude. Applications on NSTX-U will include the measurement of impurity influxes in the lower divertor strike point region and the imaging of plasma-material interaction on the head of the surface analysis probe MAPP (Material Analysis and Particle Probe). The diagnostic setup and initial results from its application on the lithium tokamak experiment are presented. © 2015 AIP Publishing LLC. [<http://dx.doi.org/10.1063/1.4935609>]

## I. INTRODUCTION

Visible imaging is widely applied for the routine monitoring of plasma discharges in magnetic fusion devices. Applications range from the study of plasma-material interaction (PMI) and identification of off-normal events (e.g., in the Joint European Torus JET,<sup>1</sup> DIII-D,<sup>2</sup> National Spherical Torus Experiment NSTX,<sup>3,4</sup> Alcator C-Mod,<sup>5</sup> Mega-Ampere Spherical Tokamak MAST,<sup>6</sup> Experimental Advanced Superconducting Tokamak EAST,<sup>7</sup> and Tore Supra<sup>8</sup>), quantitative analysis of emission from impurity or fuel atoms (e.g., in Alcator C-Mod,<sup>9</sup> DIII-D<sup>10</sup> and NSTX<sup>11</sup>), real-time control of plasma shaping (e.g., in the Tokamak à Configuration Variable TCV<sup>12</sup>), and imaging of intermittent blobby-like turbulence (e.g., in NSTX<sup>13</sup> and Alcator C-Mod<sup>14</sup>).

In fusion devices, diagnostics need to maintain reliability in nuclear environments. This can be achieved either via the installation of shielded (for neutrons and x-rays) periscopes (e.g., as on JET<sup>1</sup> and DIII-D<sup>15</sup>) or using radiation-hardened cameras. Radiation-hardened detectors based on the charge-injection device (CID) architecture<sup>16</sup> have been used for monitoring and surveillance in nuclear reactors, nuclear medicine applications, and other radiation environments. Their use in fusion devices was pioneered on DIII-D<sup>2,10</sup> (for divertor and main chamber impurity emission measurements) and recently introduced on Alcator C-Mod<sup>9</sup> (for main wall erosion studies). It must also be noted that increased neutron yields will affect image guide systems typically used in fusion devices (i.e., browning of glass fiber bundles<sup>17</sup>), which will need to be replaced with optical relay systems.<sup>1,7,15,18</sup>

Simultaneous imaging of different atomic emission lines can provide supplementary information, e.g., from spectroscopic line ratio techniques exploiting the dependence of excited state populations on local  $T_e$ ,  $n_e$ . Line ratio techniques for the determination of plasma parameters have been

applied on several fusion devices typically using neutral helium lines (e.g., on the Large Helical Device LHD,<sup>19</sup> Tokamak Experiment for Technology Oriented Research TEXTOR,<sup>20</sup> Reversed-Field eXperiment RFX<sup>21</sup> and Hybrid Tokamak HYBTOK-II<sup>22</sup>). The ionizations per photon method (S/XB),<sup>23</sup> commonly applied for the determination of impurity erosion fluxes from the measured line-integrated brightness, opens additional opportunities for PMI studies using two-wavelength imaging. These include the accurate determination of impurity influxes (monitoring different lines of the same charge state of the same impurity), the determination of gross vs. net erosion (monitoring neutral and singly ionized charged states of the same impurity), and the characterization of differences in erosion patterns of different materials (monitoring the same charge state of different impurities). Studies of main chamber wall erosion of molybdenum PFCs in C-Mod via visible imaging with an intensified CID camera<sup>9</sup> showed the need for the simultaneous imaging of atomic emission lines and nearby continuum (due to visible bremsstrahlung, Planck, and molecular emission). While this was addressed in C-Mod via imaging on and off the molybdenum emission line in two comparable discharges, simultaneous measurements are needed to avoid the need for repeated, reproducible discharges.

Several image-splitter systems are commercially available, providing simultaneous imaging at different wavelengths on a single or multiple detectors. Commercially available systems include, among others, Optosplit II by Cairn Research,<sup>24</sup> QV2 by Photometrics,<sup>25</sup> and W-VIEW GEMINI by Hamamatsu.<sup>26</sup> Two-color imaging on the same detector (side-by-side) further provides the advantage of having an intrinsic timing synchronization and allows for the use of a single camera. While simultaneous two-color imaging on the same detector is widely used in life sciences for fluorescence imaging, limited applications are found for PMI studies in fusion devices. Examples include, among others, two-color infra-red

(IR) imaging<sup>27</sup> (using the Optosplit II), ion flow measurements (using a custom-built image splitter),<sup>28</sup> and a four-wavelength helium line ratio system (using a custom built image splitter).<sup>22</sup>

Understanding the evolution of the plasma facing components (PFCs) surface conditions in the mixed material environment of the National Spherical Torus Experiment Upgrade (NSTX-U)<sup>29</sup> divertor and first wall will require simultaneous monitoring of emission from different atomic species (carbon, lithium, boron, and oxygen). Measurements of the steep radial gradients and toroidal asymmetries in emission profiles (e.g., due to tile edges and non-axisymmetric wall conditioning) will need 2D high-resolution imaging. The increase in neutron fluences (estimated to be on the order of  $1 \times 10^{16}$  neutrons for a 5 s, 2 MA discharge<sup>29</sup>), due to the increased beam power and pulse length with respect to NSTX, will eventually make radiation-hardened diagnostics a necessity. In this work, a two-channel spectral imaging system was built for the study of material erosion and surface composition evolution in the NSTX-U divertor. The system builds upon radiation-hardened imaging systems developed on DIII-D<sup>2,10</sup> and C-Mod,<sup>9</sup> introducing the possibility of simultaneous imaging on the same detector at two different wavelengths, differing in emissivity up to three orders of magnitude. Experimental setup on NSTX-U, calibration, and first results from the application of the system on the Lithium Tokamak Experiment (LTX)<sup>30</sup> are presented in this paper.

## II. EXPERIMENTAL SETUP ON NSTX-U

Understanding the evolution of the mixed-material divertor environment in NSTX-U will require simultaneous 2D imaging of different atomic species. NSTX-U PFCs include ATJ-grade and POCO graphite tiles. Boronization<sup>31</sup> (via deuterated tri-methyl-borane, D-TMB) and lithium evaporative coatings<sup>32</sup> will be the main methods for the conditioning of the wall PFCs. Recently, the increased oxygen uptake was identified in test stand experiments<sup>33</sup> as a possible mechanism responsible for the enhanced deuterium retention on lithiated graphite. Steep radial gradients in emission profiles, radially varying particle fluxes and coating erosion, toroidal asymmetries in divertor lithium influxes due to asymmetry in evaporated coatings make the case for 2D (radial and toroidal) high-resolution imaging. The dynamic environment of boron and lithium coatings under the high ion fluxes of the NSTX-U divertor (several  $10^{23}$  ion/m<sup>2</sup>/s) and the role of conditioning history on PFCs conditions will limit the applicability of repeated discharges for the evaluation of mixed-material evolution. The two-wavelength imaging system (TWICE, Two-Wavelength Imaging Camera Equipment) was therefore developed to image the lower divertor PFCs in NSTX-U and expand the capabilities available from fast visible cameras<sup>3</sup> with the ability to image weaker visible lines (via an image intensifier) and the simultaneous imaging of the same field of view at different wavelengths. Applications under consideration for testing in NSTX-U include the following.

- Characterization of gross vs. net erosion for different atomic species in the mixed material environment (lithium, carbon, and boron), monitoring different

charge states of same impurity (neutral and singly ionized, via the S/XB method<sup>34</sup>).

- Determination of impurity influxes independent from local plasma parameters ( $T_e$ ,  $n_e$ ) from line ratio of different emission lines from same charge state.
- Determination of plasma parameters via spectroscopic line ratio techniques using neutral helium and lithium line ratios.
- Investigation of the role of oxygen in regulating lithiated graphite behavior in a tokamak environment via simultaneous monitoring of lithium and oxygen emission.
- Characterization of the erosion pattern of materials typically difficult to image with non-intensified visible cameras: oxygen, boron, molybdenum, tungsten, and comparison with lithium and carbon.

Concerning the last point, in particular, NSTX-U has a long term plan of transitioning from graphite PFCs to high-Z metallic PFCs. The conversion is scheduled to start in 2016 with the replacement of the second row of the outer divertor tiles in the lower divertor with TZM molybdenum tiles. Imaging of molybdenum erosion has proven challenging due to the weak emission in the visible spectrum and the consequent importance of continuum emission (bremsstrahlung, molecular, Planck emission).<sup>9</sup> Demonstrated capabilities in the imaging of molybdenum erosion with CID cameras on C-Mod,<sup>9</sup> enhanced by two-wavelength capabilities, make TWICE ideally suited to help in the characterization of impurity influxes from the future installation of metallic PFCs in NSTX-U.

### A. Viewing geometry on NSTX-U

Two different views were developed for TWICE in NSTX-U, addressing two critical areas of the lower divertor: the first aimed at the strike point region and the second aimed at the *in situ* surface analysis sample probe MAPP (Material Analysis and Particle Probe)<sup>35</sup> in the far scrape-off layer (SOL). Port locations on NSTX-U for both views can be reached via an imaging fiber bundle from the TWICE stand.

The first view was developed for the imaging of the outer strike point area. A re-entrant view-port, similar to the one discussed in Ref. 3, was installed on one of the top ports and complements the other 2D lower divertor views for fast visible cameras<sup>3</sup> (respectively, 30° and 120° away). The re-entrant view-port consists of a 6.625-in. long pipe (2.5-in. in internal diameter) with a 2-in. sapphire window, welded to a 6-in. flange (see Figure 1(a) for a picture of the window from inside the NSTX-U vessel). A remotely controlled rotary feed-through is used to actuate a shutter and protect the window during lithium evaporation. The collection optics is inserted in the re-entrant view-port by means of a lens holder manufactured in Delrin resin, and views the plasma through a gap in the PFC tiles at a major radius ( $R$ ) of 105 cm on the top of NSTX-U (as shown in Figure 1). The tilt and the focal length of the imaging optics were chosen to image the area of the lower divertor corresponding to the position of the inner and outer divertor legs in discharges with high and

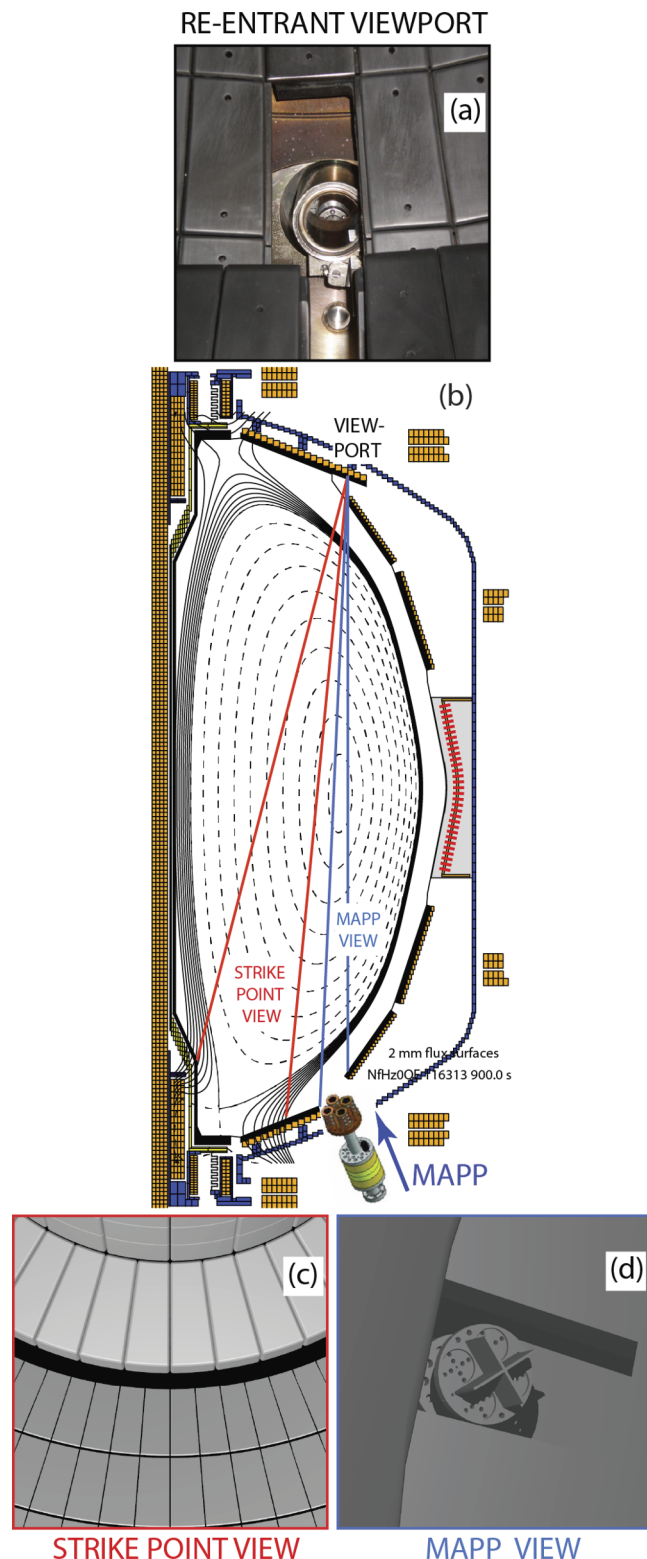


FIG. 1. Picture of the re-entrant window taken from the inside of the NSTX-U vessel (a). Poloidal cross section of the NSTX-U vacuum vessel with TWICE fields of view (b): OSP in red and MAPP in blue. TWICE fields of view on NSTX-U as rendered using the ray-tracing code POV-Ray<sup>36</sup>: OSP (c) and MAPP (d).

medium shapings (i.e., outer strike point radii  $R_{OSP} \sim 45$ – $75$  cm). For this purpose, a 25 mm, F/1.4 C-mount lens was chosen providing a field of view of  $50 \times 50$  cm on the coherent optical fiber bundle used as image guide. The imaging bundle

is a  $4 \times 4$  mm in cross section, 15-foot-long coherent imaging fiber bundle (Schott IG-154) consisting of  $400 \times 400$   $8/10 \mu\text{m}$  glass fibers (core/cladding) with a numerical aperture (NA) of 0.63 assembled in multi-fiber bundles ( $6 \times 6$  fibers) and transmitting wavelengths longer than 400 nm. Figure 1 shows the field of view from the poloidal cross section of the NSTX-U vacuum vessel (b) and as rendered with the ray tracing software POV-Ray<sup>36</sup> (c). The field of view covers the inner and outer strike points (ISP and OSP, typically on the vertical and horizontal tiles, respectively) and provides imaging of a toroidal angle of about  $30^\circ$  with a spatial resolution of the order of 1 mm/pixel.

A second view was developed for the imaging of the MAPP.<sup>33</sup> The MAPP is a surface analysis sample system, equipped with X-ray photoelectron spectroscopy (XPS) and thermal desorption spectroscopy (TDS) instruments. MAPP can expose samples of PFC materials to a plasma for analysis *in situ*, providing information on surface composition and main chemical reaction mechanisms. MAPP will be operational in the NSTX-U lower outer divertor area from 2015 and will expose samples to the plasma through one of the gaps in the PFC tiles at a radius of 105 cm. A view of the MAPP head was developed using a 75 mm F/2.5 lens in the same re-entrant view-port used for one of the wide angle views of the lower divertor<sup>3</sup> and toroidally separated  $30^\circ$  from the MAPP location. The MAPP view will have a field of view of  $\sim 15 \times 15$  cm allowing a resolution of  $\sim 0.3$  mm/pixel. A rendering of the MAPP view via POV-Ray is shown in Figure 1(d) with the MAPP head (without samples) inserted in the NSTX-U vacuum vessel. Both views (wide and MAPP) will be available at the same time with two fiber bundles inserted in the re-entrant port. The MAPP view, combined with surface science analysis will provide unique opportunities for comparison of elemental composition and its evolution inferred from sputtering measurements and surface spectroscopy (XPS).

## B. Experimental setup and detector characterization

An image-splitting optical setup was designed by means of commercially-available mechanically-referenced optical components to allow for the imaging of light emitted by the plasma at two different wavelengths side-by-side on the same detector. Schematic and pictures of the image-splitter box and detector are shown, respectively, in Figures 2 and 3. The light collected by the imaging optics focused at the NSTX-U divertor is relayed by the fiber bundle to the image-splitter optics box. The image-splitter box is enclosed in a light-tight aluminum and hard blackboard enclosure installed on an aluminum optical breadboard. All the optics and optomechanical components exploit the Thorlabs<sup>37</sup> cage mount system to guarantee mechanically-referenced alignment and sturdy setup. The light relayed by the imaging bundle to the image-splitter box is collimated by a 50 mm F/2.3 C-mount lens focussed at infinity and rigidly mounted to an antireflection-coated 1-in. beam splitting cube (50-50 transmission) which splits the image in the two optical paths. Two filter wheels (Thorlabs) are rigidly mounted to the beamsplitter cube on each optical path. Each filter wheel can hold up to six

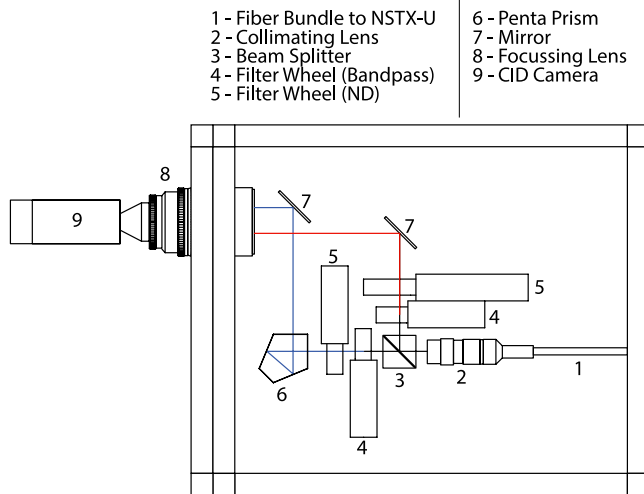


FIG. 2. Layout of optical and mechanical components in the image-splitter box.

1-in. filters. The first filter wheel in each optical path is loaded with narrow bandpass filters while the second one is used for the neutral density filters. Absorptive antireflection-coated 1-in. neutral density filters (Schott glass) are utilized with neutral

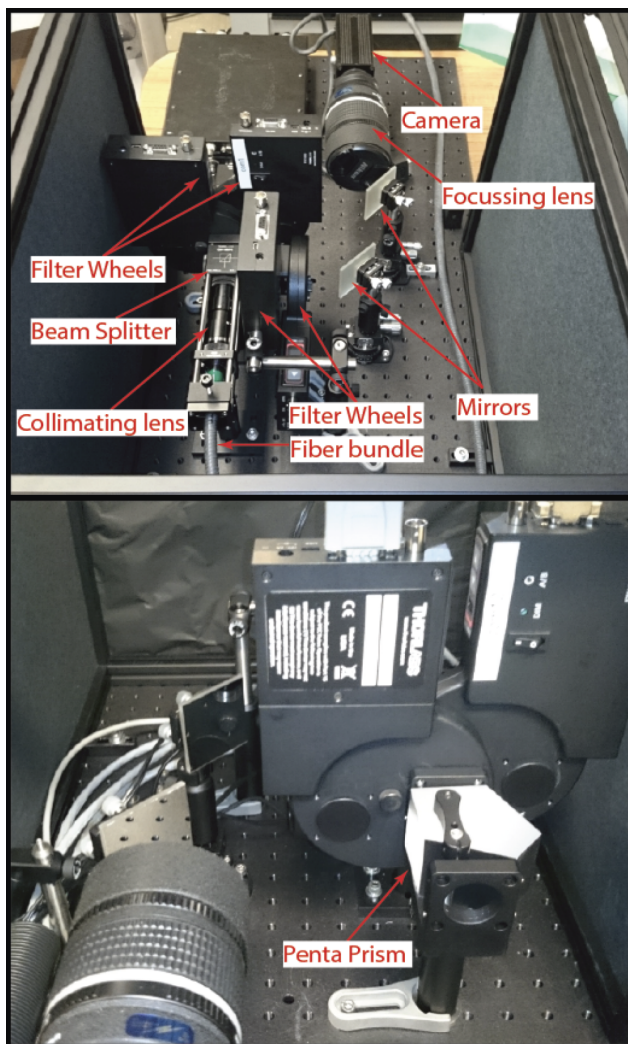


FIG. 3. Pictures of the image-splitter box setup.

TABLE I. Narrow bandpass interference filters used in the TWICE setup and relative atomic transitions.

Filter	$\lambda$ (nm)	FWHM (nm)	Transition
Li I	670.9	1.5	$1s^2 2s-1s^2 2p$
Li I	610.4	1.5	$1s^2 2p-1s^2 3d$
Li I	460.3	1.0	$1s^2 2p-1s^2 4d$
Li II	548.5	1.6	$1s 2s-1s 2p$
C II	514.4	3.5	$2s 2p 3s-2s 3 p 3 p$
C II	426.7	1.2	$2s^2 3d-2s^2 4f$
CD band	429.5	3.0	$A^2 \Delta-X^2 \Pi$
C III	465.0	1.5	$1s^2 2p 3s-1s^2 2 p 3 p$
D- $\beta$	486.0	1.4	$n=2$ to $n=4$
O II	441.6	1.3	$2s^2 2p^2 3s-2s^2 2 p^2 3 p$
W I	400.9	1.2	$5d^3 6s-5d^3 6p$
Mo I	550.8	0.95	$4d^5 5s-4d^5 5p$
B I	563.0	1.0	$2s^2 3s-2s^2 4p$
B II	703.0	5.0	$1s^2 2s 3s-1s^2 2s 3 p$
B III	449.8	1.0	$1s^2 4d-1s^2 5f$

densities (ND) up to 3.0. This allows for comparable counts on the sensor with differences in line brightness up to a factor of 1000 in the two paths and roughly covers an attenuation comparable to the gain offered by the intensifier. Bandpass filters (Andover<sup>38</sup>) used in the setup include the filters shown in Table I.

The filter wheels are controlled via the RS-232 serial interface. Remote operation is allowed by means of a serial server (Digi PortServer<sup>39</sup>) which adds Ethernet connectivity to the serial devices. The first optical path is flipped horizontally by a cage-mounted penta prism (uncoated N-BK7 glass, 28 × 28 mm in clear aperture) and both paths are then directed to the focussing optics by two 1-in. square silver mirrors on adjustable (rotary + linear) stages with side-mounted micrometers, which allow for the easy alignment of the system. Light is finally focussed on the detector by means of a Nikon 135 mm F/2.0 lens, coupled at infinity.

The detector is a radiation-hardened CID CID8710D1M camera by ThermoScientific.<sup>16</sup> The camera is equipped with a 2/3-in. 8-bit 755 × 484 pixel sensor with 12 × 13.7  $\mu\text{m}$  pixels. The detector provides sensitivity in the near-UV with quantum efficiency above 10% at 200 nm and is equipped with an image intensifier (Photonis GENII-UV, P43 phosphor). The intensifier is coupled to the detector via a fiberoptic quartz (Suprasil) taper providing a demagnification of 1.6. The gate duration can be adjusted from 20 ns to 16.2 ms. Both gain and gate duration can be controlled remotely via RS-485 serial connection. The CID camera has a 30 Hz frame rate and outputs a RS-170 2:1 interlaced analog signal. The camera can operate in magnetic fields up to 0.03 T.

An external frame grabber iPORT Analog-Pro by Pleora<sup>40</sup> was used to digitize the signal with a 720 × 480 pixels resolution. The external frame grabber converts the analog RS-170 signal to a GigE vision compliant stream with up to two analog inputs per frame grabber. The GigE vision signal is acquired by a Gigabit Ethernet (GbE) network interface card (NIC) on the controlling PC. Python<sup>41</sup> software based on a commercially available ActiveGigE software development kit (SDK) by A&B software<sup>42</sup> was developed to couple the acqui-

sition and the gating to the MDSPPlus<sup>43</sup> based shot cycle. USB-powered oscilloscope (Syscomp<sup>44</sup> Circuitgear CGR-101) and waveform generator (Syscomp<sup>44</sup> Advanced Waveform Generator WGM-201) controlled by the Python acquisition software were used for hardware triggering and external gating control. De-interlacing of the GigE Vision stream is performed in post-processing leading to an effective 60 Hz frame rate with halved vertical spatial resolution.

An absolute 2D calibration, including image flat field correction, was performed as a function of gain, bandpass, and neutral density filter by means of an integrating sphere in order to allow for the quantitative analysis of camera images. The sensor response was found to be linear within a few percent as a function of both gate duration and signal intensity, as plotted in Figure 4 for three different gain settings. The detector linearity eases absolute calibration and quantitative analysis of experimental data. The gain adjustment of the image intensifier provides a gain of up to a factor of 3000 as shown in Figure 5, where the sensor response was tested as a function of the gain setting. This allows for the imaging of weak emission lines and drove the choice of ND filters employed in the setup. Intensifier gain scans at constant detector counts (compensating gain with ND filters) were performed to characterize signal-to-noise level of the detector at different gain settings. In Figure 6, the variance in the pixel count estimated over 90 frames is plotted for different intensifier gain settings as a function of the average pixel count on the detector. Linear fits at each gain setting show distributions of photoelectrons

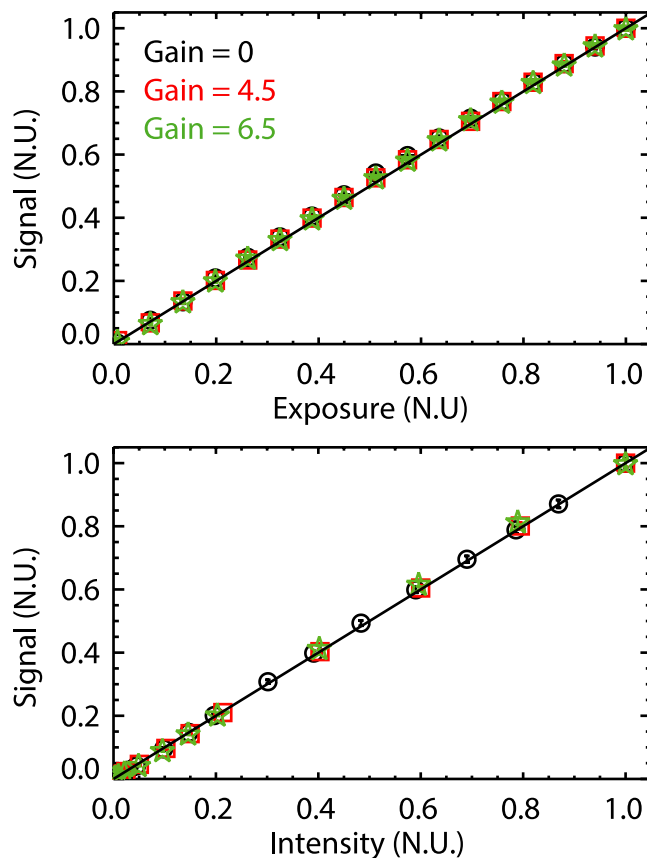


FIG. 4. Linearity response of detector as a function of gate duration (top) and signal intensity (bottom) for different gain settings.

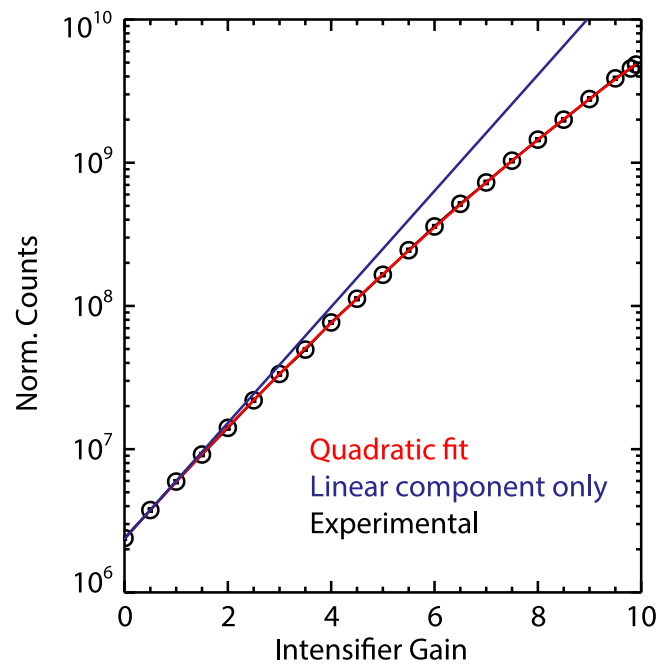


FIG. 5. Background-subtracted detector counts as a function of image intensifier gain. Quadratic fit (and the linear component only) to the linear-logarithmic plot of the gain curve is also overlaid.

at the photocathode of the micro-channel plate characteristic of Poisson statistics.<sup>45</sup> The increase in the slope for increasing gain setting shows the increase in the number of photoelectrons per count. A constant offset of about 30 counts and dark noise of about 0.5 counts were found independently of exposure time and gain setting. For low values of the gain (below 6.0), the noise level was found not to degrade the dynamic range provided by the digitization.

Two easily interchangeable configurations of the image-splitter box were developed to either maximize the field of view imaged on the sensor or the filled area of the sensor. The choice of the optics was driven by the minimization of vignetting, the minimization of broadening and central wavelength blue-shift of the bandpass filter, the ease of setup on the cage system, the minimization of light loss, and the needed magnification. This led to the choice of 1-in. optics with a compromise between long focal lengths and etendue conservation. Two different configurations were used for the collimating optics, always using the 135 mm lens as focussing optics. The first configuration used a 50 mm F/2.3 lens and was used to fill the vertical dimension of the sensor maximizing the filled area on the detector. This configuration has a magnification of 1.7 (including the effect of the glass taper) and a fill factor of 100%. While part of the fiber bundle is not imaged on the sensor, the use of the penta prism allows for the same area to be imaged for the two light paths at all the times on the sensor. The second configuration used a slower 75 mm F/3.9 lens to fill the horizontal dimension of the sensor, minimizing the area of the bundle not imaged on the detector. This configuration has a magnification of 1.12 and a fill factor of about 68%. While the same magnification could have been achieved with coupled lenses with shorter focal lengths, this configuration was chosen to avoid any vignetting and bandpass shift of the bandpass

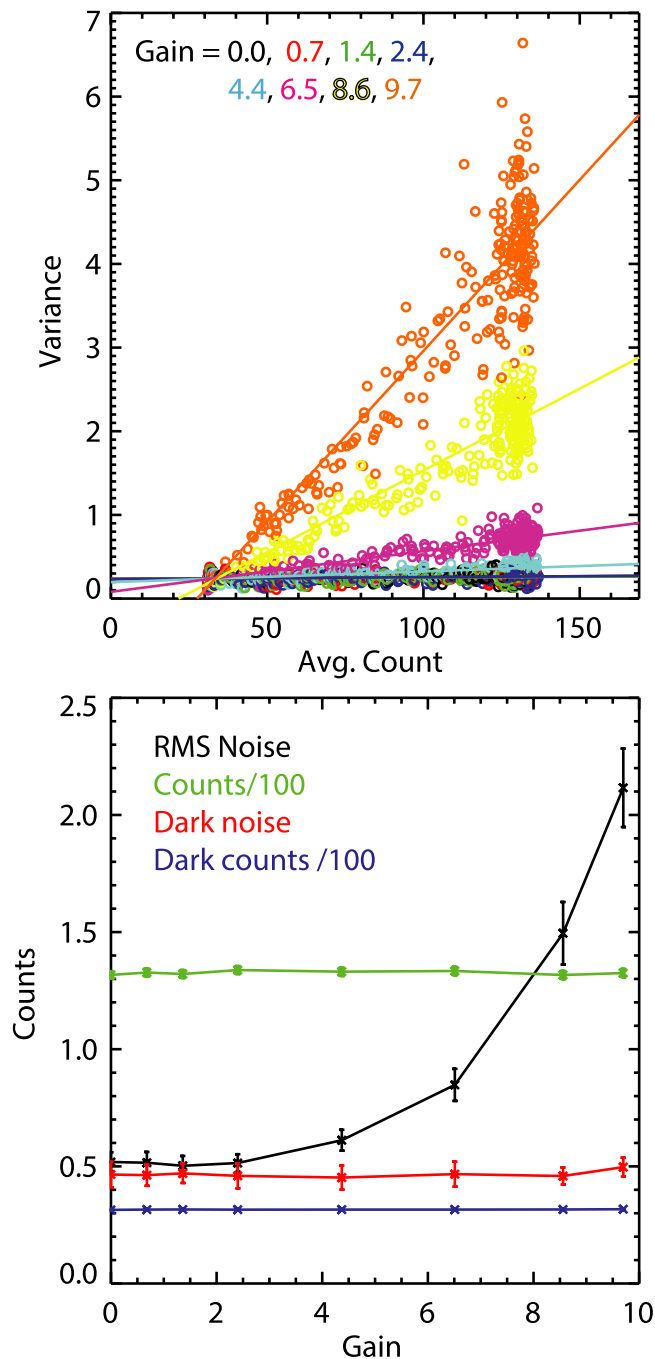


FIG. 6. Top: Variance in the pixel count (over 90 frames) for different intensifier gain settings as a function of the average pixel count on the detector and linear fit. Bottom: Noise, dark current, and dark noise as a function of gain setting evaluated for constant counts on the detector.

filters, with the drawback of some loss of light. Images from the two available configurations, while the collection optics were imaging a target, are shown in Figure 7.

### III. INITIAL RESULTS

Initial results exploiting the two-wavelength imaging capabilities were obtained on the LTX<sup>46</sup> at the Princeton Plasma Physics Laboratory (PPPL), where TWICE was installed for initial testing. LTX is a small-sized tokamak with the physics purpose of studying plasma operation with liquid

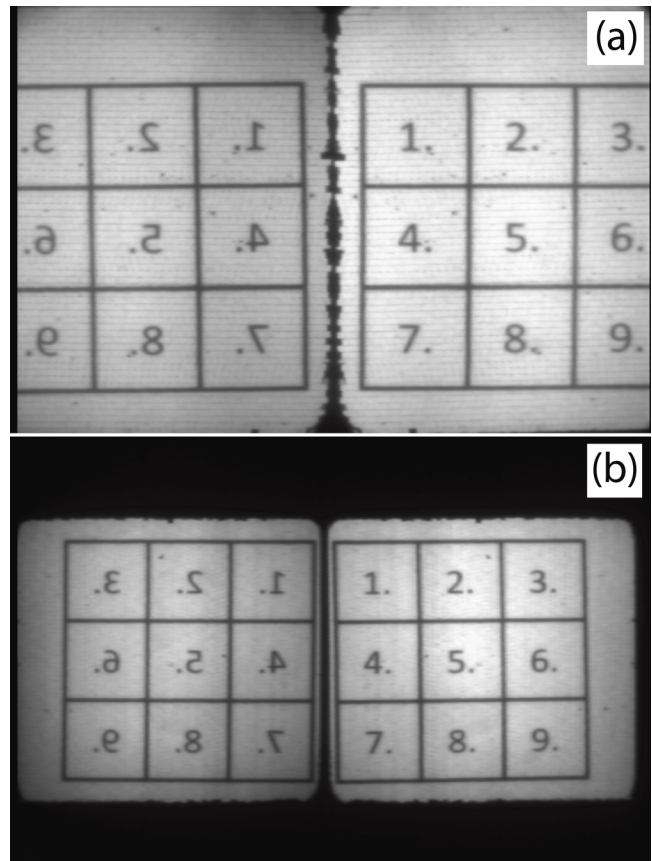


FIG. 7. Target imaged with the two different configurations of the image-splitter box optics: (a)—filling the vertical dimension of the sensor and (b)—filling the horizontal dimension of the sensor.

lithium PFCs. The main engineering and plasma parameters are major radius  $R = 0.4$  m, minor radius  $a = 0.26$  m, on-axis toroidal field  $B_T \leq 0.2$  T, plasma current  $I_p \leq 80$  kA, discharge duration  $t \leq 40$  ms, and stored energy  $W_{MHD} \leq 300$  J. Heatable copper shells lined with stainless steel and coated with lithium form limiting surfaces that are conformal to the plasma. Lithium is routinely evaporated onto the shells via electron-beam heating of a pool of lithium introduced into the bottom of shell segments via a crucible.<sup>47</sup> Two views were developed on midplane ports in LTX to test different applications for the two-wavelength imaging capabilities of this system. These two applications include the imaging of the LTX high field side (HFS) limiter and the imaging of the MAPP head<sup>35</sup> on LTX and are presented in Sec. III A and Sec. III B, respectively.

#### A. Imaging of the LTX HFS limiter

Simultaneous imaging of a limiting PMI surface through emission from the main low-Z conditioning material and surface contaminants can provide information on the evolution of the PFCs surface conditions. A view of the HFS limiter was obtained through a window on a 2-3/4-in. flange on the low field side (LFS) midplane with a radial line-of-sight focussed on the HFS stainless steel shell. A 50 mm F/1.4 lens was used as the collection optics. The view, which was focussed off-line at the nominal distance between the window and the HFS

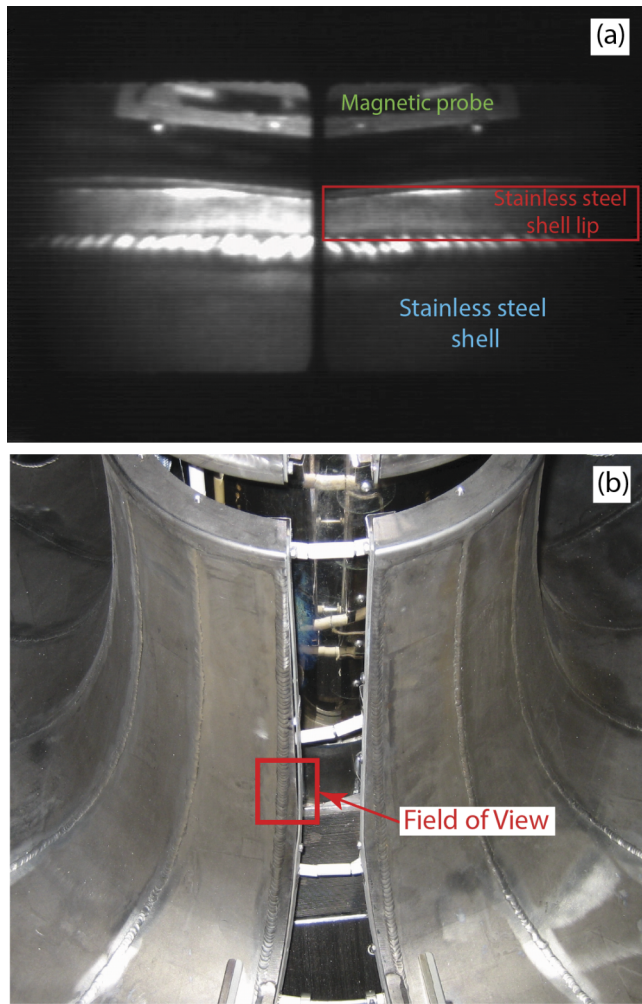


FIG. 8. (a) HFS LTX limiter imaged by TWICE (without interference filters) as illuminated by the in-vessel tungsten filament. (b) Picture of the inboard side of the LTX shells with a red box overlaid to indicate the TWICE field of view shown in (a).

shell, is shown in Figure 8(a) as imaged by TWICE (without interference filters) while the limiter was illuminated by the in-vessel tungsten filament: one can observe the stainless steel shell, the limiter lip, and a magnetic probe located in the gap behind the shells. A picture of the inboard side of the LTX shells is shown in Figure 8(b). A red box is overlaid to indicate the TWICE field of view imaged in Figure 8(a). The discharges presented in this section were performed after one month without plasma operation and without fresh wall conditioning. The walls were therefore expected to be passivated (by oxygen and carbon) lithium surfaces as lithium coatings are typically observed to passivate in the LTX background vacuum within a few days even without plasma operation. For the imaging of the HFS limiter, emission from low charged-states of carbon and lithium was simultaneously monitored (C II 514 nm and Li I 670.8 nm with ND 2.0). Given the LTX discharge duration, typically only three of the 60 Hz de-interlaced frames contain information. The light was integrated over the entire discharge, noting that comparable information was obtained from each frame.

A decrease in the ratio of carbon to lithium emission from the PFCs was observed as the plasma conditioned the limiter

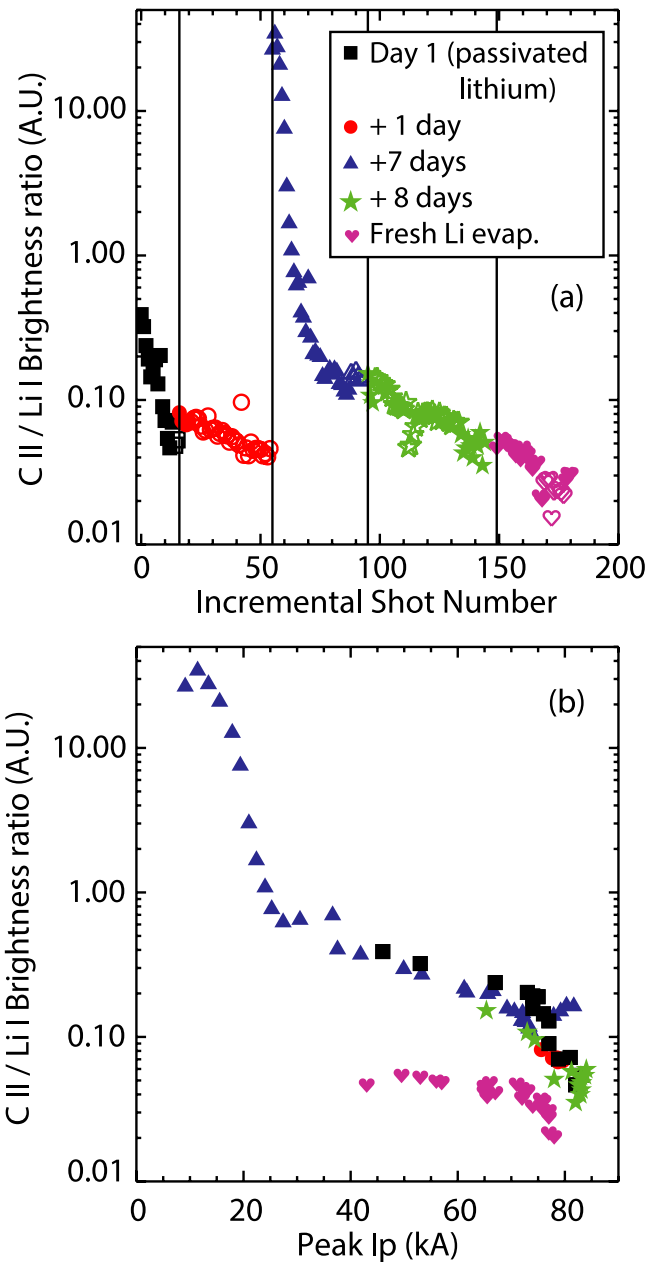


FIG. 9. Evolution of the C II (514 nm)/Li I (670 nm) ratio with progressive discharges on unconditioned walls for consecutive run days (January 22—black, January 23—red, January 29—blue, January 30—green, February 18—pink) as a function of the incremental shot number (top) and of the peak achieved plasma current (bottom). Filled and empty symbols represent discharges with different Ohmic coils programming.

surface. The ratio of C II to Li I emission ( $R_{C/Li}$ , which can be representative of the ratio of carbon to lithium influx from the limiter) is plotted in Figure 9(a) versus the incremental shot number from five consecutive run days (January 22 in black, January 23 in red, January 29 in blue, January 30 in green and February 18 in pink) after a month without operation. Filled and empty symbols indicate shots with different Ohmic (OH) coils programming. It can be observed that  $R_{C/Li}$  decreases continuously during the first day of operation (black symbols) by up to an order of magnitude. After overnight passivation, a small increase in  $R_{C/Li}$  was observed and this was followed by a continuous decrease during the day (red symbols). Following



FIG. 10. Color camera picture of MAPP probe inserted in the LTX vacuum vessel as illuminated from the vessel filaments.

a week without operation, passivation of the PFCs was again observed with a large increase of the carbon to lithium ratio followed by a steady decrease during the two following operation days (blue and green symbols). Comparable values for  $R_{C/Li}$  in discharges with comparable wall conditions but different coil programming (and  $I_p$ ) indicate that this ratio can be representative of the wall conditions rather than plasma parameters. Discharges after a fresh lithium evaporation are also included with pink symbols, showing a decrease in  $R_{C/Li}$  below the levels achieved with passivated coatings. In Figure 9(b),  $R_{C/Li}$  is now plotted versus the peak  $I_p$  in the discharge, for discharges with the same coil programming. A correlation between the achieved plasma current and  $R_{C/Li}$  is observed. This suggests that the improvement in the plasma performance can be related to the progressive cleaning of the wall surface, which exposes the lithium underneath. A clear difference can also be observed for the discharges with fresh lithium evaporation which show, for comparable plasma currents, a reduction of over a factor of 2 in  $R_{C/Li}$ .

### B. Imaging of the MAPP probe head on LTX

Concomitant analysis of elemental composition from surface science and spectroscopic analysis can be a powerful way to understand the PFC conditions. The MAPP was used on LTX during 2014 and was inserted in the LFS SOL during discharges, at a radial location such that the samples would be flush with the outboard shell limiting surface, as shown in

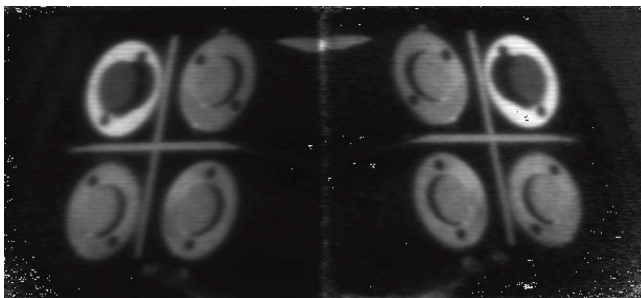


FIG. 11. View of the MAPP head as imaged by TWICE and illuminated by the in-vessel tungsten filament. One of the four samples (top-left sample in the left image) underwent TDS analysis and was partially depleted of its lithium coverage, appearing different under vessel filament illumination.

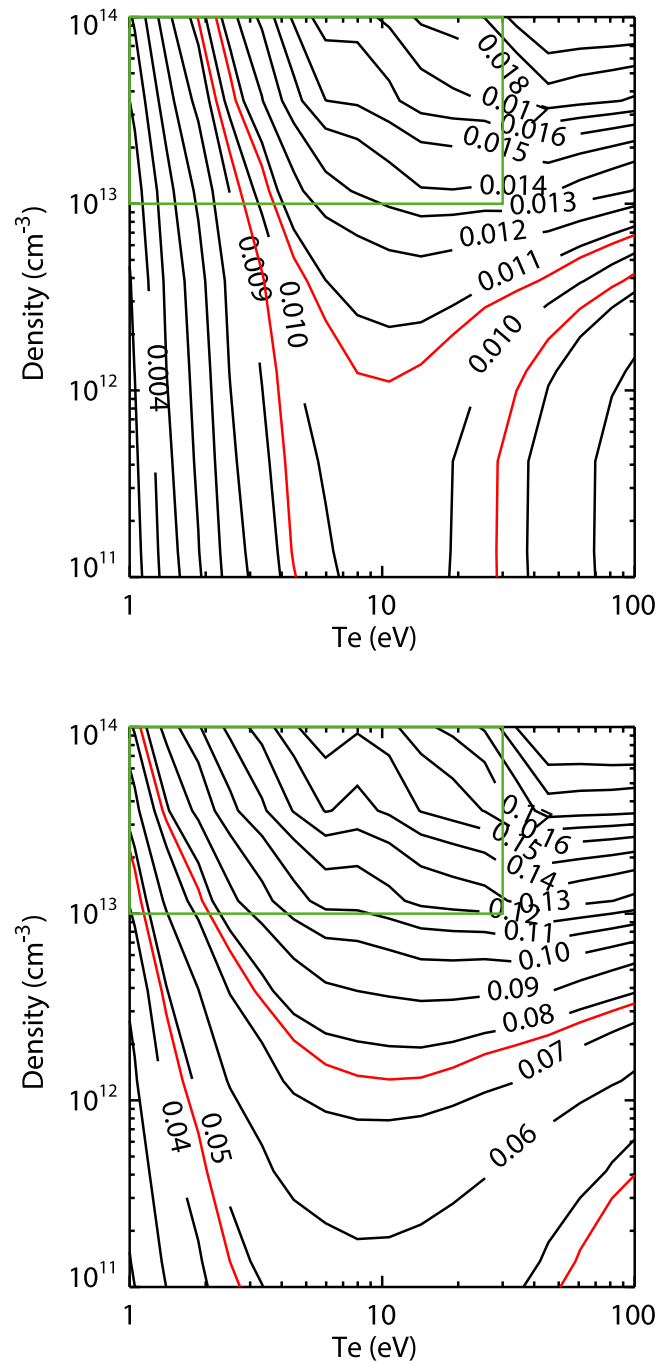


FIG. 12. Contour plot of the ratio of excitation photon emission coefficients for the lithium line ratios 460 nm/670 nm (top) and 610 nm/670 nm (bottom). The experimental values are overlaid as red contours. Divertor plasma parameters expected in NSTX-U are indicated with a green box.

Figure 10. A view imaging the head of the MAPP probe was obtained through a midplane window on a 6-in. flange. For the imaging of the MAPP head, a 100 mm F/2.8 C-mount lens was chosen providing a field of view of  $2 \times 2$  in. on the  $4 \times 4$  mm bundle. A view of the MAPP head illuminated by the vessel filament and imaged by TWICE is shown in Figure 11. The MAPP head contains 4 samples, each of which can undergo surface analysis via XPS or TDS in a separate chamber. A Langmuir probe is also installed in the head and operated as a single probe. In the exposure to LTX plasmas, all the samples consisted of stainless steel.

Over two run days with fresh lithium evaporation, the MAPP head was imaged via H $\beta$ , O II and Li I bandpass filters to explore possible applications of combined surface and spectroscopic analysis. Three neutral lithium lines (460, 610, and 670 nm) were alternated in two filter configurations in repeated discharges. This was done to attempt the determination of electron temperature ( $T_e$ ), density ( $n_e$ ), and neutral lithium influxes via the lithium line ratios technique. Photoemission coefficients from the ADAS database<sup>48</sup> were used to determine the map of expected Li I ratios as a function of  $T_e$ ,  $n_e$  (Figure 12). Line ratios were evaluated from the emission over each sample in the frame with peak emission. The range of line ratios experimentally observed in comparable discharges analyzed is overlaid in red to the contour plots in Figure 12. In the  $T_e$  and  $n_e$  regimes of the SOL plasmas in LTX, only a weak dependence on the plasma parameters is observed. The overlap of the regions identified by the two line ratios in comparable discharges indicates  $n_e \leq 1 \times 10^{12} \text{ cm}^{-3}$  and  $T_e \sim 5\text{--}25 \text{ eV}$ , allowing an estimate of average gross eroded neutral lithium flux on the MAPP sample of approximately  $3\text{--}6 \times 10^{19} \text{ atoms/m}^2/\text{s}$ . For the NSTX-U divertor conditions, indicated with green boxes in Figure 12, stronger sensitivity of the line ratios on  $n_e, T_e$  is observed which could further reduce the uncertainties associated with this technique.

#### IV. CONCLUSIONS

A two-channel spectral imaging system based on a charge injection device radiation-hardened intensified camera was built for the imaging of divertor PFCs in NSTX-U. In this paper, the setup and detector characterization for NSTX-U are presented together with initial results from its application on LTX. Applications included the evaluation of the evolution of the limiter surface conditions and of the lithium line ratio technique to infer neutral lithium influxes.

#### ACKNOWLEDGMENTS

The authors would like to thank Dr. R. E. Bell and A. L. Roquemore for useful discussions, Dr. S. L. Allen, Dr. M. E. Fenstermacher, Dr. B. Stratton, and Dr. R. Kaita for diagnostic support, Professor J. P. Allain for useful discussions and MAPP support, A. Brereton for engineering drawings, and Dr. R. Majeski, Dr. J. Schmitt, D. Boyle, M. Lucia, and the rest of the LTX Team for help in the setup and for LTX operation. The digital data for this paper can be found in <http://arks.princeton.edu/ark:/88435/dsp018p58pg29j>. This work was supported by U.S. DOE Contract Nos. DE-AC02-09CH11466 and DE-AC52-07NA27344.

<sup>1</sup>A. Huber, S. Brezinsek, P. Mertens, B. Schweer, G. Sergienko, A. Terra, G. Arnoux, N. Balshaw, M. Clever, T. Edlingdon, S. Egner, J. Farthing, M. Hartl, L. Horton, D. Kampf, J. Klammer, H. T. Lambert, G. F. Matthews, C. Morlock, A. Murari, M. Reindl, V. Riccardo, U. Samm, S. Sanders, M. Stamp, J. Williams, K. D. Zastrow, C. Zauner, and JET EFDA Contributors, *Rev. Sci. Instrum.* **83**, 10D511 (2012).

<sup>2</sup>M. E. Fenstermacher, W. H. Meyer, R. D. Wood, D. G. Nilson, R. Ellis, and N. H. Brooks, *Rev. Sci. Instrum.* **68**, 974 (1997).

<sup>3</sup>F. Scotti, A. L. Roquemore, and V. A. Soukhanovskii, *Rev. Sci. Instrum.* **83**, 10E532 (2012).

<sup>4</sup>A. L. Roquemore, T. Biewer, D. Johnson, S. J. Zweben, and N. Nishino, *Rev. Sci. Instrum.* **75**, 4190 (2004).

<sup>5</sup>C. J. Boswell, J. L. Terry, B. Lipschultz, and J. Stillerman, *Rev. Sci. Instrum.* **72**, 935 (2001).

<sup>6</sup>A. Patel, P. G. Carolan, N. J. Conway, C. A. Bunting, and R. J. Akers, *Rev. Sci. Instrum.* **75**, 4145 (2004).

<sup>7</sup>J. H. Yang, X. F. Yang, L. Q. Hu, Q. Zang, X. F. Han, C. Q. Shao, T. F. Sun, H. Chen, T. F. Wang, F. J. Li, and A. L. Hu, *Rev. Sci. Instrum.* **84**, 085102 (2013).

<sup>8</sup>A. Geraud, S. Salasca, J. M. Verger, T. Alarcon, G. Agarici, S. Bremond, J. P. Chenevois, M. Geynet, J. B. Migozzi, and C. Reux, *Rev. Sci. Instrum.* **80**, 033504 (2009).

<sup>9</sup>A. N. James, D. Brunner, B. Labombard, C. Lau, B. Lipschultz, D. Miller, M. L. Reinke, J. L. Terry, C. Theiler, G. M. Wallace, D. G. Whyte, S. Wukitch, and V. Soukhanovskii, *Plasma Phys. Controlled Fusion* **55**, 125010 (2013).

<sup>10</sup>M. Groth, R. M. Ellis, N. H. Brooks, M. E. Fenstermacher, C. J. Lasnier, W. H. Meyer, and J. M. Moeller, *Rev. Sci. Instrum.* **80**, 033505 (2009).

<sup>11</sup>F. Scotti, V. A. Soukhanovskii, J. W. Ahn, R. E. Bell, S. P. Gerhardt, M. A. Jaworski, R. Kaita, H. W. Kugel, A. G. McLean, E. T. Meier, M. Podestá, and A. L. Roquemore, *J. Nucl. Mater.* **463**, 1165 (2015).

<sup>12</sup>G. Hommen, M. de Baar, B. P. Duval, Y. Andrebe, H. B. Le, M. A. Klop, N. J. Doelman, G. Witvoet, M. Steinbuch, and TCV Team, *Nucl. Fusion* **54**, 073018 (2014).

<sup>13</sup>S. J. Zweben, R. J. Maqueda, D. P. Stotler, A. Keesee, J. Boedo, C. E. Bush, S. M. Kaye, B. LeBlanc, J. L. Lowrance, V. J. Mastrocola, R. Maingi, N. Nishino, G. Renda, D. W. Swain, J. B. Wilgen, and NSTX Team, *Nucl. Fusion* **44**, 134 (2004).

<sup>14</sup>J. L. Terry, S. J. Zweben, K. Hallatschek, B. LaBombard, R. J. Maqueda, B. Bai, C. J. Boswell, M. Greenwald, D. Kopon, W. M. Nevins, C. S. Pitcher, B. N. Rogers, D. P. Stotler, and X. Q. Xu, *Phys. Plasmas* **10**, 1739 (2003).

<sup>15</sup>C. J. Lasnier, S. L. Allen, R. E. Ellis, M. E. Fenstermacher, A. G. McLean, W. H. Meyer, K. Morris, L. G. Seppala, K. Crabtree, and M. A. Van Zeeland, *Rev. Sci. Instrum.* **85**, 11D855 (2014).

<sup>16</sup>Thermo Fisher Scientific, Inc., <http://www.thermoscientific.com/>.

<sup>17</sup>A. Islamov, E. Ibragimova, and I. Nuritdinov, *J. Nucl. Mater.* **362**, 222 (2007).

<sup>18</sup>S. S. Medley, *Rev. Sci. Instrum.* **70**, 794 (1999).

<sup>19</sup>M. Goto, *J. Quant. Spectrosc. Radiat. Transfer* **76**, 331 (2003).

<sup>20</sup>B. Schweer, M. Brix, and M. Lehnen, *J. Nucl. Mater.* **266–269**, 673 (1999).

<sup>21</sup>L. Carraro, M. E. Puiatti, F. Sattin, P. Scarin, and M. Valisa, *Rev. Sci. Instrum.* **72**, 967 (2001).

<sup>22</sup>N. Ohno, K. Miyamoto, K. Kodama, S. Kajita, and K. Kitagawa, *Contrib. Plasma Phys.* **50**, 962 (2010).

<sup>23</sup>K. Behringer, *J. Nucl. Mater.* **145–147**, 145 (1987).

<sup>24</sup>Cairn Research Limited, <http://www.cairn-research.co.uk/>.

<sup>25</sup>Photometrics, <http://www.photometrics.com/>.

<sup>26</sup>Hamamatsu, <http://www.hamamatsu.com/>.

<sup>27</sup>A. G. McLean, J.-W. Ahn, R. Maingi, T. K. Gray, and A. L. Roquemore, *Rev. Sci. Instrum.* **83**, 053706 (2012).

<sup>28</sup>S. F. Paul and N. Nishino, 47th Annual Meeting of the American Physical Society, 2005.

<sup>29</sup>J. E. Menard, S. Gerhardt, M. Bell, J. Bialek, A. Brooks, J. Canik, J. Chrzanowski, M. Denault, L. Dudek, D. Gates, N. Gorelenkov, W. Guttenfelder, R. Hatcher, J. Hosea, R. Kaita, S. Kaye, C. Kessel, E. Kolemen, H. Kugel, R. Maingi, M. Mardenfeld, D. Mueller, B. Nelson, C. Neumeyer, M. Ono, E. Perry, R. Ramakrishnan, R. Raman, Y. Ren, S. Sabbagh, M. Smith, V. Soukhanovskii, T. Stevenson, R. Strykowski, D. Stutman, G. Taylor, P. Titus, K. Tresemer, K. Tritz, M. Viola, M. Williams, R. Woolley, H. Yuh, H. Zhang, Y. Zhai, A. Zolfaghari, and NSTX Team, *Nucl. Fusion* **52**, 083015 (2012).

<sup>30</sup>R. Majeski, L. Berzak, T. Gray, R. Kaita, T. Kozub, F. Levinton, D. Lundberg, J. Manickam, G. Pereverzev, K. Snieckus, V. Soukhanovskii, J. Spaleta, D. Stotler, T. Strickler, J. Timberlake, J. Yoo, and L. Zakharov, *Nucl. Fusion* **49**, 055014 (2009).

<sup>31</sup>C. H. Skinner, H. W. Kugel, R. Maingi, W. R. Wampler, W. Blanchard, M. G. Bell, R. E. Bell, D. A. Gates, S. M. Kaye, P. LaMarche, B. P. LeBlanc, J. E. Menard, D. Mueller, H. K. Na, N. Nishino, F. Paoletti, S. F. Paul, S. A. Sabbagh, V. A. Soukhanovskii, and D. Stutman, *Nucl. Fusion* **42**, 329 (2002).

<sup>32</sup>H. W. Kugel, M. G. Bell, J.-W. Ahn, J. P. Allain, R. E. Bell, J. Boedo, C. Bush, D. Gates, T. K. Gray, S. Kaye, R. Kaita, B. P. LeBlanc, R. Maingi, R. Majeski, D. Mansfield, J. E. Menard, D. Mueller, M. Ono, S. Paul, R.

- Raman, A. L. Roquemore, P. W. Ross, S. A. Sabbagh, H. Schneider, C. H. Skinner, V. A. Soukhanovskii, T. Stevenson, J. Timberlake, W. R. Wampler, and L. Zakharov, *Phys. Plasmas* **15**, 056118 (2008).
- <sup>33</sup>C. Taylor, J. Dadras, K. Luitjohan, J. Allain, P. Krstic, and C. Skinner, *J. Appl. Phys.* **114**, 223301 (2013).
- <sup>34</sup>K. Behringer, H. P. Summers, B. Denne, M. Forrest, and M. Stamp, *Plasma Phys. Controlled Fusion* **31**, 2059 (1989).
- <sup>35</sup>C. N. Taylor, B. Heim, S. Gonderman, J. P. Allain, Z. Yang, R. Kaita, A. L. Roquemore, C. H. Skinner, and R. A. Ellis, *Rev. Sci. Instrum.* **83**, 10D703 (2012).
- <sup>36</sup>Persistence of Vision Raytracer Pty, Ltd., P.O. Box 407, Williamstown, Victoria 3016, Australia, <http://www.povray.org/>.
- <sup>37</sup>Thorlabs, Inc., <https://www.thorlabs.com/>.
- <sup>38</sup>Andover Bandpass Filters, [www.andover.com](http://www.andover.com).
- <sup>39</sup>DIGI PortServer, <http://www.digi.com/products/serialservers/>.
- <sup>40</sup>Pleora Technologies, Inc., <http://www.pleora.com/>.
- <sup>41</sup>Python, <https://www.python.org/>.
- <sup>42</sup>A&B Software LLC, <http://www.ab-soft.com/>.
- <sup>43</sup>MDSPlus, <http://www.mdsplus.org/>.
- <sup>44</sup>Syscomp, <http://www.syscompdesign.com/>.
- <sup>45</sup>R. E. Bell, D. W. Johnson, B. C. Stratton, and E. J. Synakowski, *Rev. Sci. Instrum.* **63**, 4744 (1992).
- <sup>46</sup>R. Majeski, T. Abrams, D. Boyle, E. Gransteadt, J. Hare, C. M. Jacobson, R. Kaita, T. Kozub, B. P. LeBlanc, D. P. Lundberg, M. Lucia, E. Merino, J. Schmitt, D. Stotler, T. M. Biewer, J. M. Canik, T. K. Gray, R. Maingi, A. G. McLean, S. Kubota, W. A. Peebles, P. Beiersdorfer, J. H. T. Clementson, and K. Tritz, *Phys. Plasmas* **20**, 056103 (2013).
- <sup>47</sup>J. C. Schmitt, R. E. Bell, D. P. Boyle, B. Esposti, R. Kaita, T. Kozub, B. P. LeBlanc, M. Lucia, R. Maingi, R. Majeski, E. Merino, S. Punjabi-Vinoth, G. Tchilingirian, A. Capece, B. Koel, J. Roszell, T. M. Biewer, T. K. Gray, S. Kubota, P. Beiersdorfer, K. Widmann, and K. Tritz, *Phys. Plasmas* **22**, 056112 (2015).
- <sup>48</sup>H. P. Summers, The ADAS User Manual, version 2.6, 2004, <http://www.adas.ac.uk>.